Title

Spark Plasma Sintering of Non-Thermal Plasma Synthesized Silicon Carbonitride Nanoparticles

Authors

Herzberg, Steven
Edwards, Joshua
Dupuy, Alexander
et al.

Publication Date

2024-05-28

Spark Plasma Sintering of Non-Thermal Plasma Synthesized Silicon Carbonitride Nanoparticles

Steven Herzberg[1], Joshua Edwards[2], Alexander Dupuy[3,4] Lorenzo Mangolini[1], Suveen Mathaudhu[1,2]

[1]University of California, Riverside
[2]Colorado School of Mines
[3]University of California, Irvine
[4]University of Connecticut

Abstract

Amorphous silicon carbonitride (SiCN) has significant potential as a high-temperature structural material, however, current reports on its synthesis suggest a lack of methods to limit its devitrification into crystalline phases. In this work, non-thermal plasma synthesis and high-pressure spark plasma sintering (SPS) are used to produce bulk, dense SiCN samples. An applied uniaxial pressure of 500 MPa with a soak temperature at 1600 °C produced SiCN with a Vickers hardness up to 16.1 GPa, fracture toughness of 2.6 MPa·$m^{1/2}$, and Young's Modulus up to 247 GPa. XRD and DSC showed that SiCN stayed primarily amorphous through the sintering process; however, some SiC nanocrystalline domains formed within the amorphous matrix. Electron microscopy shows a lack of pores, but with pockets of the Y_2O_3 dispersed among the SiCN. Archimedes' measurements of samples sintered at 1400 °C and 1600 °C determined the density of the samples to be 3.02 and 3.21 g/cm^3, respectively. The results suggest the potential for using amorphous plasma, synthesized nanoparticles and spark plasma sintering to produce bulk amorphous or composite ceramic materials with novel stoichiometry and properties.

Introduction

Amorphous silicon carbonitride (SiCN) has demonstrated promise for future high-temperature applications such as turbine blades and thermal barrier coatings. In addition to good room temperature mechanical properties for an engineering ceramic such as high hardness,[1–3] amorphous SiCN possesses excellent oxidation resistance and creep resistance at temperatures up

to 1300 °C.[5,7] Meanwhile, traditional engineering ceramics such as SiC and Si_3N_4 begin to volatize and oxidize above 1200 °C, converting these materials into mechanically weaker SiO_2. Creep causes cavitation at these temperatures as well, which drives crack formation and propagation.[4] Studies by An *et al.* have shown amorphous SiCN to have a steady-state creep rate too small to be effectively measured at 1280 °C,[5] contrasting with the creep behavior of commonly used engineering ceramics. For example, Si_3N_4 has been reported to have a steady state strain rate of approximately 10^{-8} s^{-1} under similar testing conditions.[6] Raj *et al.* have measured amorphous SiCN to have a parabolic rate constant for oxidation as 1.1×10^{-18} to 3.8×10^{-18} m^2/s at 1350 °C in ambient air and notes that this oxidation behavior is significantly lower than sintered SiC and Si_3N_4 reported from other literature.[7]

SiCN is commonly produced through polymer pyrolysis, whereby polymer pre-ceramics such as polysilanes and polycarbosilanes undergo shaping, cross-linking, and pyrolysis.[8] However, this process results in an open porous material due to outgassing byproducts such as hydrogen and hydrocarbons preventing pore closure.[9] An alternative method to achieve full density SiCN is through pulverization of pyrolyzed, porous SiCN into a powder through ball milling, followed by sintering through hot pressing or spark plasma sintering (SPS) to densify the powder into bulk. However, ball milling has been known to introduce contaminants into the milled materials.[10] In excessive amounts, impurities can negatively impact the structural properties of SiCN by forming mechanically weaker phases. In addition, it is challenging to produce fully densified amorphous SiCN as the sintering temperature and crystallization temperature are both nominally 1500 °C, at which point amorphous SiCN precipitates into a crystalline SiC/Si_3N_4 nanocomposite.[11] As a result, most published works that engage in sintering SiCN are in actuality making SiC/Si_3N_4 composites.[3, 12–15]

Recently, our group has described an alternative path towards the fabrication of amorphous SiCN that circumvents some of these issues. This involves the production of SiCN nanopowders through non-thermal plasma synthesis.[16] In short, gaseous precursors are used to produce contaminant-free amorphous SiCN nanopowders in a continuous process. In addition, it was shown that varying the gas flow rate ratios of the precursors controlled the composition of the SiCN, including what phases were present after thermal treatment. This led to an amorphous SiCN phase with an increased resistance to crystallization at temperatures exceeding 2000 °C. Attempts at sintering of the plasma-synthesized SiCN nanopowders were unsuccessful due to the outgassing of N_2 at 1500 °C. We have found that this inhibits sintering, leading to poor mechanical performance.

Two general approaches to overcome the outgassing problem have been tested. One method is to sinter in a pressurized atmosphere of N_2 (1-5 bar) to suppress the outgassing of N_2 from the SiCN.[20] The other method is to use high pressure sintering, where a uniaxial pressure ranging from a few hundred MPa to 1 GPa is applied during sintering to engage early onset sintering.[13] The latter approach reduces the temperature needed to achieve full density to below the outgassing temperature of N_2 of 1500°C. In this work, we explore the high-pressure spark plasma sintering of non-thermal plasma synthesized amorphous SiCN nanoparticles at 500 MPa and 1600 °C with goal of fully densifying non-thermal plasma synthesized amorphous SiCN without complete devitrification. We then compare the mechanical properties of the resultant compacts with those reported in the literature for other bulk synthesis approaches.

Methods & Materials

SiCN nanoparticles were produced through non-thermal plasma synthesis using gaseous precursors with the following flow rates: SiH_4+Ar (1.37% SiH_4) at 640 sccm, CH_4 at 10 sccm, and

NH_3 at 8 sccm. The design of the system (Figure 1a.) was based on previous work.[16] Non-thermal plasmas are versatile systems for the production of nanoparticles,[17] with recent reports confirming that they are good sources of ceramic-based nanomaterials as well.[18, 19] The first stage contains a capacitively coupled plasma generated using a radio frequency (13.56 MHz) power supply. The second stage consists of an MTI OTF-1200X tube furnace where the nanoparticles are passed through to remove excess hydrogen.[21] An in-flight annealing stage is important; without it, excess hydrogen on the surface of the SiCN nanoparticles outgasses during sintering and becomes trapped in pores, impeding sintering. The plasma is run at a power of 100 W at a pressure of 3 torr, while the tube furnace is set to 1000 °C. The nanoparticles (Figure 1b) were collected on a stainless-steel mesh filter placed after the tube furnace. To prevent oxygen contamination of the SiCN, the filter with nanoparticles was pressurized to atmospheric pressure with argon before being sealed and transferred to an argon glovebox. While in the glovebox, the nanoparticles are extracted from the

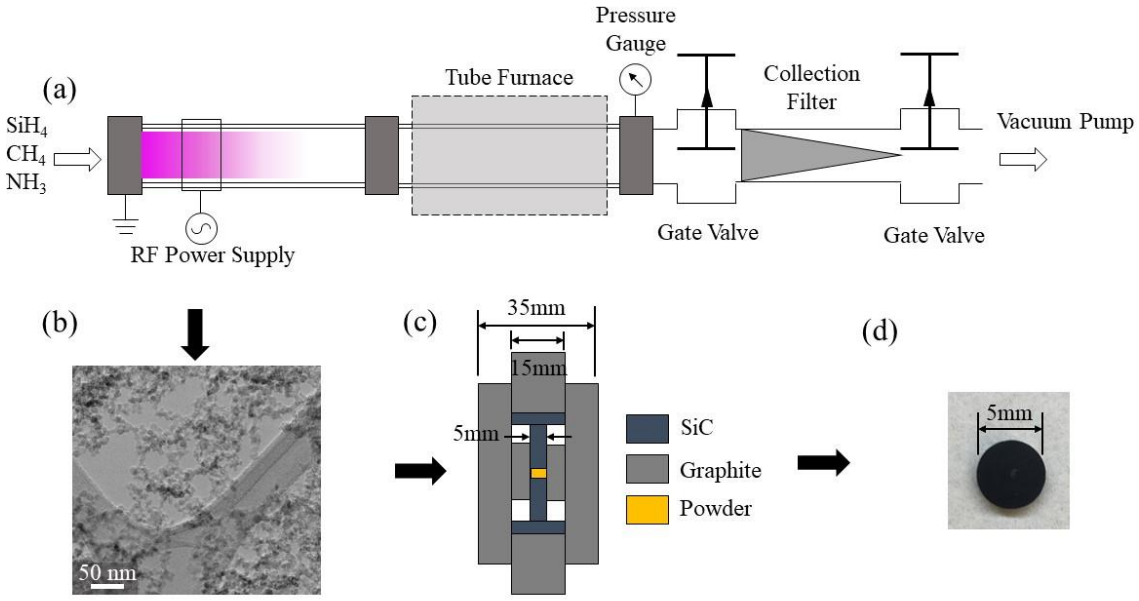

Figure 1. (a) Schematic of non-thermal plasma synthesis system. (b) TEM of collected SiCN nanoparticles. (c) Schematic of the high pressure SiC+graphite punch and die setup used to sinter amorphous SiCN nanoparticles under 500 MPa of pressure. (d) Sintered SiCN disk.

filter and mixed with a 15 wt% Y_2O_3 sintering aid in a tumbler overnight. The Y_2O_3 induces liquid phase sintering, where the sintering aid melts and flows in between the particles. Part of the solid SiCN particles go into solution in the Y_2O_3 melt, forming an oxynitride liquid phase. This creates a solution-precipitation process with faster interparticle diffusion compared to the evaporation-condensation process that occurs when no sintering aids are used.[12, 22] However, the Y_2O_3 was observed to stay in the material after sintering and the relatively low melting point in comparison to SiCN reduces the mechanical performance at high temperatures.

Spark plasma sintering of the SiCN nanoparticles was carried out with a Fuji Electronic Industrial SPS-515. For each sample, 0.1 g of the SiCN nanoparticles were pressed into a 5 mm diameter high pressure sintering punch and die set consisting of graphite and SiC components, the design of which is shown in Figure 1c. Nominal temperature is measured using a pyrometer aimed at the top outer punch. The temperature of the inner die during sintering is estimated to be approximately 200 °C colder than the point the pyrometer measures. The estimation was determined by a dry run up to 1000 °C comparing the readings of the pyrometer aimed at the top outer punch and thermocouple inserted through a hole in the outer die and in contact with the inner die, with the temperature offset extrapolated to the target temperatures. Subsequently, all reported temperatures are of the estimated inner die temperature. The samples were sintered under vacuum at 1400 °C and 1600 °C, with a heating rate of 150 °C/min, soaked at temperature for 30 min, and cooled at a rate of 100 °C/min. During sintering, the samples were initially held at 600 °C (the lower limit of the pyrometer) under minimal applied pressure to allow remnant hydrogen still on the SiCN nanoparticles to outgas before pore closure at higher temperatures, the regular ramp rate up to the soak temperature was continued once the SPS chamber pressure returned to its initial state (~3Pa), signaling that the outgassing has stopped. The SiCN powders are densified under 500

MPa of uniaxial pressure applied once the soak temperature is reached. After sintering, the SiCN are black, crack-free disks (Figure 1d).

After sintering, samples are extracted from the die, mounted in epoxy, and polished to 1 μm finish with diamond lapping pads. The samples are then characterized with X-Ray diffraction (XRD) performed on a Malvern PANalytical Empyrean Series 2 with a CuK_α source to detect crystalline phases that may form during sintering. A ThermoFisher Scientific NNS450 Scanning Electron Microscope (SEM) is used with Energy Dispersive X-Ray Spectroscopy (EDS) to observe the microstructure and determine the extent of phase segregation during sintering. The bulk density of the sintered SiCN samples is measured using the Archimedes' Method with propylene glycol as the submersion media.

Differential scanning calorimetry (DSC) was used to determine what reactions were occurring during sintering. A SiCN sample was scanned in a Netzsch DSC 404 F3 Pegasus to determine the crystallization temperature. The SiCN samples were placed in an Al_2O_3 crucible with a disk of graphite foil in between the sample and the crucible to prevent a reaction between the two. A run under the same conditions was undertaken with just the graphite foil and the crucibles to establish a background which was subsequently corrected for in the scan with SiCN. A ramp rate of 10 °C/min and a hold at 1550 °C for 10 min under an Ar atmosphere was used. The sample was scanned several times as the initial scan detected a continuous endothermic trend throughout the entire temperature range, obscuring the crystallization peaks at higher temperatures, this was likely caused by remnant hydrogen outgassing.

Nanoindentation studies were performed on a Bruker Ti950 Triboindenter equipped with a NanoDMA III low-force transducer at a rate of 600 hz with a maximum load of 10 mN, a loading rate of 400 μN/s, and a diamond Berkovich indenter to measure hardness, *H*, and reduced elastic

modulus, E_r,. The indenter was calibrated on fused quartz (FQ) according to best practices for indenter correction and machine compliance, while the tip area function (TAF) was calibrated on indents ranging from 0.1-10 mN in polished 5N-pure Aluminum and allowing for varying power-law fitting constants to better account for low-load, low-displacement indentation behavior, following best practices for low-depth indentation with regards to calibration of system and indenter compliance. For all indentations, a quasi-static trapezoidal loading profile with 5 s loading/unloading periods and a 2 s quasi-static was followed, allowing for varying strain rate and depth by varying load. Four indentation tests were conducted for the SiCN samples sintered at 1400 °C and 1600 °C, comprising of 1) a varying load indentation line from 1-10 mN to establish system compliance and drift characteristics, and 2-4) grids of indents comprising of at least 30 individual indents per set space at equidistant points on the cross-section; in all cases, indents were spaced at least 10 μm apart minimize overlap of indentation stress fields.

For grid indentations, a peak load of 4 mN was identified as the local minima for thermal/compliance drift and optimal fitting to FQ calibrated indentation range (38-198 nm) (Figure 2). Routine compliance checks throughout testing and sequences of cleaning and then profiling of the Berkovich indenter tip were conducted regularly throughout testing, as tip blunting throughout testing can result in insufficient plastic deformation observed during periodic calibration standards at the indentation depths of interest. Thus, calibration checks on system compliance and transducer performance were conducted daily, and the calculated radius of curvature for the indenter tip was recorded due to tip blunting caused by repeated indentation of materials with H > 20 GPa. Hardness (H) reported here was (h_c), the tip-area function corrected hardness, derived from the projected area, while the Elastic modulus reported from the

experimental study was E_r, the (substrate-effect-corrected) reduced elastic modulus; each defined respectively defined by the Oliver-Pharr[23] method as:

$$E_r = \frac{\sqrt{\pi}}{2}\frac{S}{A} \quad (1)$$

which relates the reduced elastic modulus, E_r, to the projected contact area A, and calculated stiffness, $S = dP / dh$.

$$H = \frac{P_{max}}{A} \quad (2)$$

where A is the projected area of contact at peak load, P_{max}

$$P(h) = \alpha (h - h_f)^m \quad (3)$$

where P is the load, hf is the total elastic displacement of the indenter tip during a complete cycle of loading/unloading, and α and m are constants derived from fitting unloading-section behavior to a power function of the form. Fracture toughness was estimated using the indentation fracture method reported on by Anstis *et al.*[24]

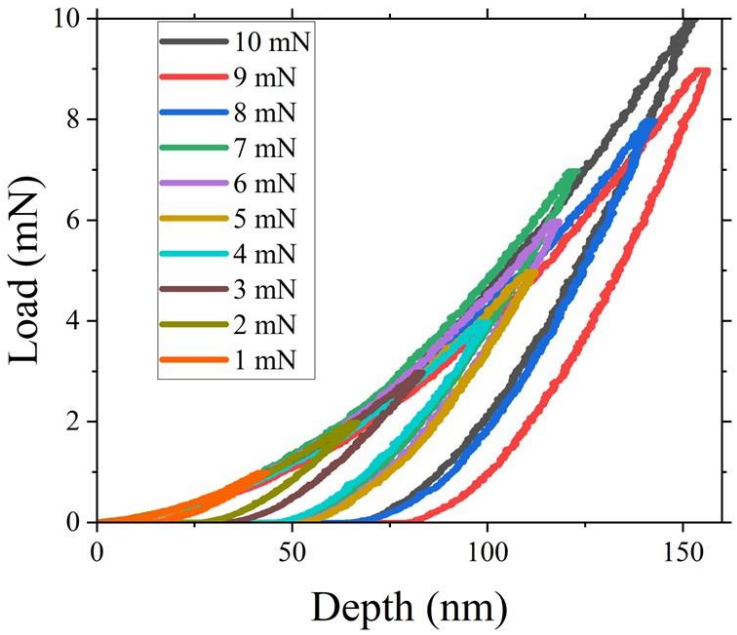

Figure 2. Loading/unloading curves with peak loads from 1mN to 10mN of SiCN sintered at 1400°C.

$$Kc = 0.016\left(\frac{E_r}{H_v}\right)^{0.5}\left(\frac{P_v}{c^{1.5}}\right) \quad (4)$$

Where K_c is the fracture toughness, H_v is Vickers hardness, P_v is the indentation load, and c is the radial crack length. The Vickers hardness was measured with a Phase II Micro Vickers Hardness Tester, Model No. 900-390 with a load of 1000 g and a dwell time of 10 sec with a minimum of 10 measurements per sample.

Results and Discussion

The X-ray diffraction pattern (Figure 3a) of plasma synthesized SiCN nanoparticles shows them to be primarily amorphous, with no discernible peaks other than a very shallow peak at 2θ = 36°, which is β-SiC's [111] lattice plane,[25] indicating the presence of some crystalline nanodomains. After sintering the SiCN at 1400 °C and 1600 °C the [111] peak sharpened and β-SiC's secondary lattice planes are now present at 2θ = 60° for [222] and 2θ = 72° for [311]. For the 1600 °C sample, α-Si_3N_4 and β-Si_3N_4 are present while the β-SiC peaks sharpen as a sign of continued crystallization at higher temperatures. α-Si_3N_4 has been reported in literature to be the first nitride phase to precipitate out of amorphous SiCN,[12, 26] and upon reaching 1500 °C α-Si_3N_4 begins to irreversibly convert to β-Si_3N_4.[27] However, the presence of peaks from both Si_3N_4 phases in the XRD pattern indicates that the α-β transition has not completed, likely due to the relatively short sintering times of SPS and the low atomic diffusivity of Si_3N_4. Further exploration of the reactions during sintering was probed via DSC of the prebaked SiCN nanoparticles (Figure 3b). At 1275 °C an exothermic trend begins, peaking at 1350 °C representing the crystallization of the SiCN into SiC/Si_3N_4 immediately followed by an endothermic rise past the baseline representing N outgassing.

Electron microscopy studies were undertaken to observe the microstructure for particle bonding, morphology, and phase separation. SEM images of the SiCN sintered at 1400 °C showed

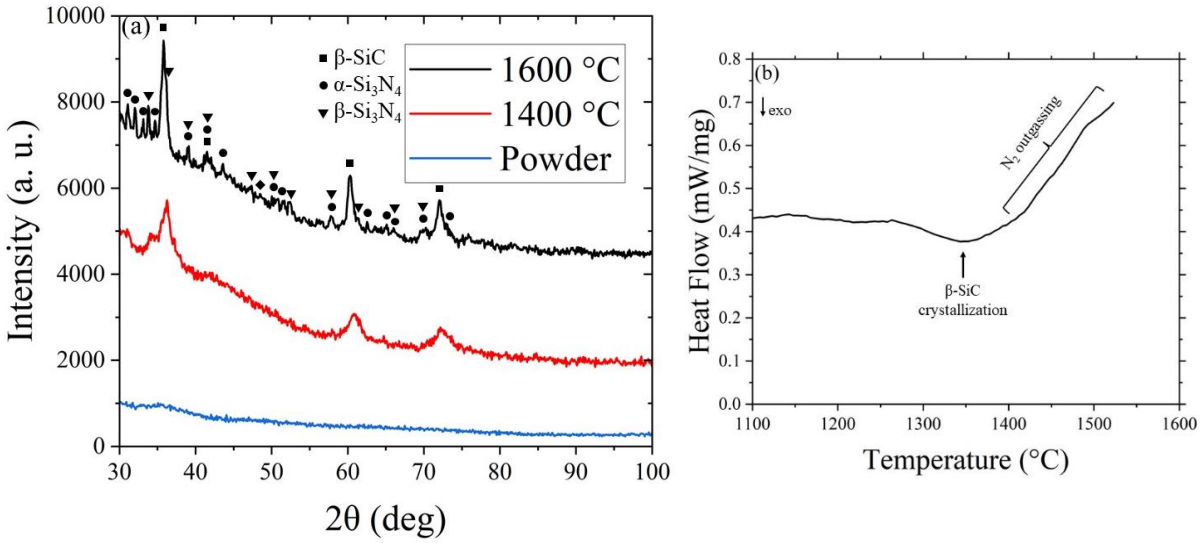

Figure 3. (a) XRD of SiCN nanoparticles before sintering and after sintering at 1400 °C and 1600 °C and SiC peaks (b) DSC of SiCN where SiC starts to crystallize at 1400 °C followed by outgassing of N_2.

noticeably lighter regions throughout the sample, which will be shown to be unintegrated Y_2O_3 sintering aid (Figure 4a). Higher magnification of the sample also indicated incomplete sintering, as clusters of unsintered nanoparticles are prevalent throughout the sample (Figure 4b). Chemical measurements via EDS show the sintered bulk SiCN to have a composition of $SiC_{0.86}N_{0.65}$ and indicates the light regions mentioned before contain high concentration of Y (pink) and O (cyan) (e.g. the Y_2O_3 sintering aid) (Figure 4e). SEM images of the SiCN processed at the higher temperature of 1600 °C did not show the same Y_2O_3 concentrated spots as the 1400 °C sample, but instead shows darker regions dispersed among lighter regions (Figure 4c). Additionally, higher magnification SEM imaging of the 1600 °C sample does not show nanoparticle clusters such as the ones present in the lower temperature sample, signaling a higher order of densification (Figure 4d). These observations point to the fact that 1400 °C, even under 500MPa, is not enough to completely sinter the SiCN nanoparticles. For the sample sintered at 1600 °C, EDS measured the composition to be $SiC_{0.76}N_{0.58}$ similar to the 1400 °C sample, although a slight reduction in N due to outgassing at the higher sintering temperature. The EDS measurement also shows the lighter

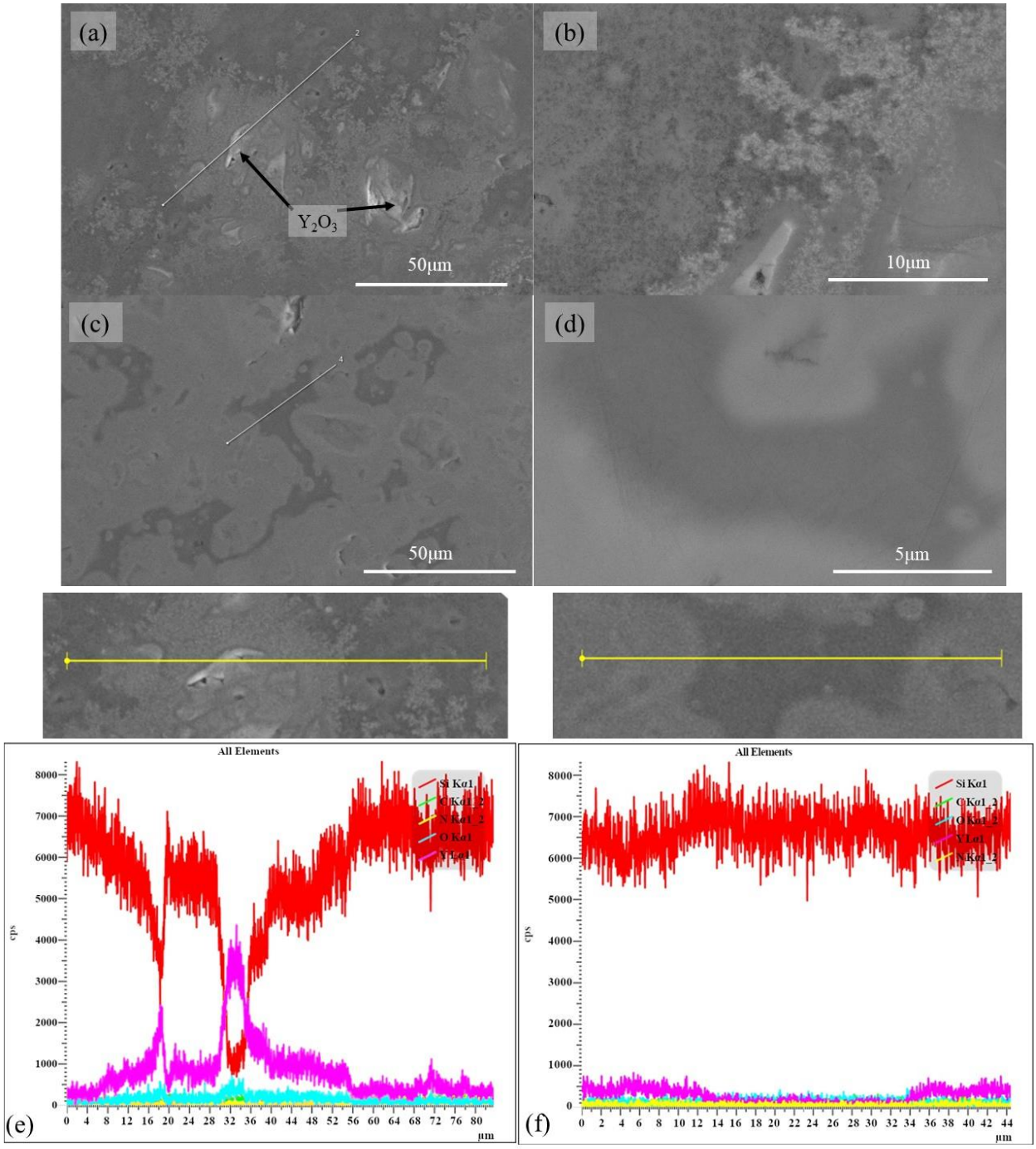

Figure 4. SEM images of SiCN sintered at 1400 °C (a) (b) and 1600 °C (c) (d). (e) EDS linescan of the 1400 °C sample shows the presence of unincorporated Y_2O_3 sintering aid likely left over as a combination of too low of a sintering temperature for too short of a time. (f) EDS linescan of the 1600 °C sample has better dispersion of the Y_2O_3, although a slight difference is still present in different regions.

regions to contain a slightly higher concentration of Y_2O_3 than the surrounding darker regions (Figure 4f), meaning the higher temperature allows for the sintering aid to more effectively dissolve and go into solution with the SiCN.

The mechanical properties of the sintered SiCN at 1400 °C and 1600 °C, as well as comparative data from literature, are shown in Table 1. The samples' Vickers hardness was measured to be 14.5 GPa and 16.1 GPa for 1400 °C and 1600 °C, respectively, within the same hardness range as other reported fully densified SiCN in literature. The lower hardness for the lower temperature sample is attributed to the incomplete densification, as discussed previously. In comparison to a similar study using SPS on plasma synthesized SiCN nanoparticles, but with a lower sinter pressure of 50 MPa which reported a maximum hardness of 1.2 GPa,[16] the increased pressure of 500 MPa shows a significant improvement on densification and the resulting

Table 1. Room temperature mechanical properties of amorphous SiCN produced through multiple methods

Sample Name	Method	Vickers Hardness (GPa)	Fracture Toughness ($MPa \cdot m^{1/2}$)	Young's Modulus (GPa)	Density (g/cm^3)	Reference
A	Warm Press (1000°C)	25	1.1	150	2.3	[1]
B	Pyrolysis (1100°C)	13	--	121	2.32	[2]
C	Pyrolysis (1050°C)	--	2.5	183	2.1	[28]
D	Pyrolysis (1050°C)	6.7	2.1	105	1.95	[29]
E	CVD†	13	--	136	--	[30]
F	Magnetron Sputtering†	18.9	--	241	--	[31]
H	SPS (1400°C, 500MPa)	14.5	2.5	235	3.02	this work
I	SPS (1600°C, 500MPa)	16.1	2.6	247	3.21	this work

mechanical properties. Young's modulus was measured to be 235 GPa and 247 GPA for the 1400 °C and 1600 °C samples, respectively. Applying the measured Young's modulus to Equation (4), the fracture toughness was calculated to be 2.5 $MPa \cdot m^{1/2}$ and 2.6 $MPa \cdot m^{1/2}$, equivalent to SiCN in other works, also shown in Table 1. The density was measured for the 1400 °C and 1600 °C samples to be 3.02 and 3.21 g/cm^3, respectively. This is higher than the reported measured density of amorphous SiCN of 2.33 g/cm^3,[1, 2] and is more in line with the density of crystalline SiC and Si_3N_4 of 3.2 g/cm^3.[14] While some crystallization is shown in XRD, the density could be interpreted to mean that complete crystallization occurred in the 1600 °C sample, possibly as crystalline nanodomains as to explain the broad peaks. As mentioned before, Figure 3a shows the 1400 °C sample contains a mixture of amorphous SiCN and nanocrystalline β-SiC, which explains its density exceeding that of amorphous SiCN. Wan *et al.* also reported a higher-than-expected density of 2.87 g/cm^3 and 2.92 g/cm^3 when sintering amorphous SiCN under 2 GPa at 1400 °C and 1600 °C, respectively.[12] With the 1400 °C sample being a mixture of amorphous and crystalline phases and the 1600 °C sample being completely crystalline. Overall, the high-pressure sintering proved effective at consolidating plasma synthesized SiCN nanoparticles, due to the lower temperatures where N_2 outgassing has less of an impact on densification, as well as the increased pressure counteracting pore growth from trapped gasses.

Conclusions

We have sintered plasma-synthesize SiCN nanoparticle to near full density using high-pressure SPS. The application of 500 MPa as opposed to a previous study that used 50 MPa provided a significant increase in density and, by extension, the mechanical properties. This brought hardness and fracture toughness up to 16.1 MPa and 2.6 $MPa \cdot m^{1/2}$, respectively, as well as a Young's Modulus of 247 MPa in line with other studies on the bulk properties of SiCN. During

sintering, partial to complete crystallization occurred, based on sintering temperature. DSC additionally shows a crystallization event occurring prior to the sintering temperatures at 1350 °C, this is associated with the formation of crystalline SiC. The comparable mechanical properties of sintered plasma-synthesized SiCN with its sintered polymer-derived counterpart demonstrates the viability for low-temperature plasma synthesis coupled with SPS for creating structural materials.

Acknowledgements

SH acknowledges support from the Department of Education's Graduate Assistance in Areas of National Need (GAANN) Fellowship program. The UCR Central Facility for Advanced Microscopy and Microanalysis (CFAMM) provided access for use of the ThermoFisher Scientific NNS450 Scanning Electron Microscope and the Malvern PANalytical Empyrean Series 2 XRD. Eric Eyerman and Brandon To from CalNano are acknowledged for carrying out the high temperature SPS processing.

Citations

1. Shah SR, Raj R. Mechanical properties of a fully dense polymer derived ceramic made by a novel pressure casting process. *Acta Materialia*. 2002;50(16):4093–4103. https://doi.org/10.1016/S1359-6454(02)00206-9
2. Galusek D, Riley FL, Riedel R. Nanoindentation of a Polymer-Derived Amorphous Silicon Carbonitride Ceramic. *Journal of the American Ceramic Society*. 2001;84(5):1164–1166. https://doi.org/10.1111/j.1151-2916.2001.tb00806.x
3. Haluschka C, Kleebe H-J, Franke R, Riedel R. Silicon carbonitride ceramics derived from polysilazanes Part I. Investigation of compositional and structural properties. *Journal of the European Ceramic Society*. 2000;20(9):1355–1364. https://doi.org/10.1016/S0955-2219(00)00010-8
4. Raj R. Fundamental Research in Structural Ceramics for Service Near 2000°C. *Journal of the American Ceramic Society*. 1993;76(9):2147–2174. https://doi.org/10.1111/j.1151-2916.1993.tb07750.x
5. An L, Riedel R, Konetschny C, Kleebe H-J, Raj R. Newtonian Viscosity of Amorphous Silicon Carbonitride at High Temperature. *Journal of the American Ceramic Society*. 1998;81(5):1349–1352. https://doi.org/10.1111/j.1151-2916.1998.tb02489.x

6. Nixon RD, Koester DA, Chevacharoenkul S, Davis RF. Steady-state creep of hot-pressed SiC whisker-reinforced silicon nitride. *Composites Science and Technology*. 1990;37(1):313–328. https://doi.org/10.1016/0266-3538(90)90107-G

7. Raj R, An L, Shah S, Riedel R, Fasel C, Kleebe H-J. Oxidation Kinetics of an Amorphous Silicon Carbonitride Ceramic. *Journal of the American Ceramic Society*. 2001;84(8):1803–1810. https://doi.org/10.1111/j.1151-2916.2001.tb00918.x

8. Colombo P, Mera G, Riedel R, Sorarù GD. Polymer-Derived Ceramics: 40 Years of Research and Innovation in Advanced Ceramics. *Journal of the American Ceramic Society*. 2010;93(7):1805–1837. https://doi.org/10.1111/j.1551-2916.2010.03876.x

9. Konetschny C, Galusek D, Reschke S, Fasel C, Riedel R. Dense silicon carbonitride ceramics by pyrolysis of cross-linked and warm pressed polysilazane powders. *Journal of the European Ceramic Society*. 1999;19(16):2789–2796. https://doi.org/10.1016/S0955-2219(99)00070-9

10. Kim SY, Choi DK, Yeo D-H, Shin HS, Yoon HG. Influence of ball milling contamination on properties of sintered AlN substrates. *Journal of the European Ceramic Society*. 2020;40(15):5349–5356. https://doi.org/10.1016/j.jeurceramsoc.2020.05.001

11. Iwamoto Y, Völger W, Kroke E, Riedel R, Saitou T, Matsunaga K. Crystallization Behavior of Amorphous Silicon Carbonitride Ceramics Derived from Organometallic Precursors. *Journal of the American Ceramic Society*. 2001;84(10):2170–2178. https://doi.org/10.1111/j.1151-2916.2001.tb00983.x

12. Wan J, Gasch MJ, Lesher CE, Mukherjee AK. High-Resolution Transmission Electron Microscopy Study of the Microstructural Development of a Silicon Carbonitride Nanocomposite. *Journal of the American Ceramic Society*. 2003;86(5):857–863. https://doi.org/10.1111/j.1151-2916.2003.tb03387.x

13. Gasch MJ, Wan J, Mukherjee AK. Preparation of a Si3N4/SiC nanocomposite by high-pressure sintering of polymer precursor derived powders. *Scripta Materialia*. 2001;45(9):1063–1068. https://doi.org/10.1016/S1359-6462(01)01140-X

14. Degenhardt U, Stegner F, Liebscher C, *et al.* Sintered silicon nitride/nano-silicon carbide materials based on preceramic polymers and ceramic powder. *Journal of the European Ceramic Society*. 2012;32(9):1893–1899. https://doi.org/10.1016/j.jeurceramsoc.2011.09.007

15. Wan J, Duan R-G, Mukherjee AK. Spark plasma sintering of silicon nitride/silicon carbide nanocomposites with reduced additive amounts. *Scripta Materialia*. 2005;53(6):663–667. https://doi.org/10.1016/j.scriptamat.2005.05.037

16. Herzberg S, Mathaudhu SN, Mangolini L. Nonthermal plasma synthesis of silicon carbonitride. *Plasma Processes and Polymers*. 2023;20(8):e2300021. https://doi.org/10.1002/ppap.202300021

17. Kortshagen UR, Sankaran RM, Pereira RN, Girshick SL, Wu JJ, Aydil ES. Nonthermal Plasma Synthesis of Nanocrystals: Fundamental Principles, Materials, and Applications. *Chem Rev*. 2016;116(18):11061–11127. https://doi.org/10.1021/acs.chemrev.6b00039

18. Coleman D, Lopez T, Yasar-Inceoglu O, Mangolini L. Hollow silicon carbide nanoparticles from a non-thermal plasma process. *Journal of Applied Physics*. 2015;117(19):193301. https://doi.org/10.1063/1.4919918

19. Exarhos S, Alvarez-Barragan A, Aytan E, Balandin AA, Mangolini L. Plasmonic Core–Shell Zirconium Nitride–Silicon Oxynitride Nanoparticles. *ACS Energy Lett*. 2018;3(10):2349–2356. https://doi.org/10.1021/acsenergylett.8b01478

20. Friess M, Bill J, Golczewski J, *et al.* Crystallization of Polymer-Derived Silicon Carbonitride at 1873 K under Nitrogen Overpressure. *Journal of the American Ceramic Society*. 2002;85(10):2587–2589. https://doi.org/10.1111/j.1151-2916.2002.tb00503.x

21. Lopez T, Mangolini L. Low activation energy for the crystallization of amorphous silicon nanoparticles. *Nanoscale*. 2014;6(3):1286–1294. https://doi.org/10.1039/C3NR02526H

22. German RM. Chapter Nine - Sintering With a Liquid Phase. In: German RM, ed. *Sintering: from Empirical Observations to Scientific Principles*. Boston: Butterworth-Heinemann; 2014:247–303. https://doi.org/10.1016/B978-0-12-401682-8.00009-4

23. Oliver WC, Pharr GM. An improved technique for determining hardness and elastic modulus using load and displacement sensing indentation experiments. *Journal of Materials Research*. 1992;7(6):1564–1583. https://doi.org/10.1557/JMR.1992.1564

24. Anstis G r., Chantikul P, Lawn B r., Marshall D b. A Critical Evaluation of Indentation Techniques for Measuring Fracture Toughness: I, Direct Crack Measurements. *Journal of the American Ceramic Society*. 1981;64(9):533–538. https://doi.org/10.1111/j.1151-2916.1981.tb10320.x

25. Ortiz AL, Sánchez-Bajo F, Cumbrera FL, Guiberteau F. X-ray powder diffraction analysis of a silicon carbide-based ceramic. *Materials Letters*. 2001;49(2):137–145. https://doi.org/10.1016/S0167-577X(00)00358-X

26. Kleebe H-J, Suttor D, Müller H, Ziegler G. Decomposition-Crystallization of Polymer-Derived Si-C-N Ceramics. *Journal of the American Ceramic Society*. 1998;81(11):2971–2977. https://doi.org/10.1111/j.1151-2916.1998.tb02722.x

27. Messier DR, Riley FL, Brook RJ. The α/β silicon nitride phase transformation. *J Mater Sci*. 1978;13(6):1199–1205. https://doi.org/10.1007/BF00544725

28. Bauer A, Christ M, Zimmermann A, Aldinger F. Fracture Toughness of Amorphous Precursor-Derived Ceramics in the Silicon-Carbon-Nitrogen System. *Journal of the American Ceramic Society*. 2001;84(10):2203–2207. https://doi.org/10.1111/j.1151-2916.2001.tb00988.x

29. Nishimura T, Haug R, Bill J, Thurn G, Aldinger F. Mechanical and thermal properties of Si–C–N material from polyvinylsilazane. *Journal of Materials Science*. 1998;33(21):5237–5241. https://doi.org/10.1023/A:1004440122266

30. Awad Y, El Khakani MA, Aktik C, *et al.* Structural and mechanical properties of amorphous silicon carbonitride films prepared by vapor-transport chemical vapor deposition. *Surface and Coatings Technology*. 2009;204(4):539–545. https://doi.org/10.1016/j.surfcoat.2009.08.032

31. Ctvrtlik R, Al-Haik MS, Kulikovsky V. Mechanical properties of amorphous silicon carbonitride thin films at elevated temperatures. *J Mater Sci*. 2015;50(4):1553–1564. https://doi.org/10.1007/s10853-014-8715-0